

1 **Tropopause Evolution in a Rapidly Intensifying Tropical Cyclone: A Static**
2 **Stability Budget Analysis**

3 Patrick Duran* and John Molinari

4 *University at Albany, State University of New York, Albany, NY*

5 **Corresponding author address:* Department of Atmospheric and Environmental Sciences, Univer-
6 sity at Albany, State University of New York, 1400 Washington Avenue, Albany, NY.

7 E-mail: pduran2008@gmail.com

ABSTRACT

⁸ We have some cool results!

9 **1. Introduction**

10 Perhaps introduce upper-tropospheric static stability and its relationship to the diurnal cycle
11 before going into Patricia? Include references to Dunion, Navarro, and O'Neill here.

12 After undergoing a remarkably rapid intensification (RI), Hurricane Patricia (2015) set a new
13 record as the strongest tropical cyclone (TC) ever observed in the Western Hemisphere (Kim-
14 berlain et al. 2016; Rogers et al. 2017). High-altitude dropsonde observations taken during
15 the Tropical Cyclone Intensity (TCI) Experiment captured this RI in unprecedented detail (Doyle
16 et al. 2017). These observations revealed remarkable changes in the structure of the cold-point
17 tropopause and upper-level static stability as the storm intensified (Duran and Molinari 2018). At
18 tropical storm intensity, shortly before RI commenced, a strong inversion layer existed just above
19 Patricia's cold-point tropopause, which was located near 17.2 km. During the first half of the RI
20 period, this inversion layer weakened throughout Patricia's inner core, with the weakening most
21 pronounced over the developing eye. By the time the storm reached its maximum intensity, the
22 inversion layer over the eye had disappeared almost completely, which was accompanied by an
23 increase in the tropopause height to a level at or above the highest-available dropsonde data point
24 (18.3 km) at two locations. Meanwhile over the eyewall region, the static stability re-strengthened
25 and the tropopause was limited to a level at or below 17.5 km. The mechanisms that led to these
26 changes in upper-level static stability and tropopause height are the subject of the current paper.

27 More recently, Dunion et al. (2014) documented a periodic oscillation of infrared brightness
28 temperature in hurricanes, which they call the "TC diurnal pulse." There will be a whole bunch of
29 papers cited here...

30 At some point (probably in the Discussion) mention the possible importance of static stability
31 asymmetries, in the context of the Dunion diurnal pulse

2. Model Setup

The numerical simulations were performed using version 19.4 of Cloud Model 1 (CM1) described in Bryan and Rotunno (2009). The equations of motion were integrated on a 3000-km-wide, 30-km-deep axisymmetric grid with 1-km horizontal and 250-m vertical grid spacing. The computations were performed on an f -plane at 15°N latitude, over a sea surface with constant temperature of 30.5°C, which matches that observed near Hurricane Patricia (2015; Kimberlain et al. 2016). Horizontal turbulence was parameterized using the Smagorinsky scheme described in Bryan and Rotunno (2009, pg. 1773), with a prescribed mixing length that varied linearly from 100 m at a surface pressure of 1015 hPa to 1000 m at a surface pressure of 900 hPa. This formulation allows for realistically-large horizontal mixing lengths near the hurricane’s inner core, consistent with the results of Bryan (2012), while not over-representing horizontal turbulence in convection at outer radii. Vertical turbulence was parameterized using the formulation of Markowski and Bryan (2016, their Eq. 6), using an asymptotic vertical mixing length of 100 m. A Rayleigh damping layer was applied outside of the 2900-km radius and above the 25-km level to prevent spurious gravity wave reflection at the model boundaries. Microphysical processes were parameterized using the Thompson et al. (2004) microphysics scheme and radiative heating tendencies were computed every two minutes using the Rapid Radiative Transfer Model for GCMs? (RRTMG) longwave and shortwave schemes (Iacono et al. 2008). A horizontally-homogeneous temperature and humidity field was initialized with a mean sounding computed using all dropsondes deployed during the TCI flight conducted within and around Tropical Storm Patricia on 21 October, 2015 (see Doyle et al. 2017 for details.) Above 19 km, where few TCI observations were available, the temperature profile was taken from the Climate Forecast System Reanalysis (CFSR) grid point nearest Patricia’s storm center, valid at 18 UTC 21 October, 2015. Since relative humidity mea-

surements were unreliable at temperatures below -40°C (Bell et al. 2016), relative humidity was set equal to 50% above 11.5 km (the level above which temperature dropped below -40°C). The vortex described in Rotunno and Emanuel (1987, their Eq. 37) was used to initialize the wind field, setting all parameters equal to the values used therein.

3. Budget Computation

The static stability can be expressed as the squared Brunt Väisälä frequency:

$$N_m^2 = \frac{g}{T} \left(\frac{\partial T}{\partial z} + \Gamma_m \right) \left(1 + \frac{T}{R_d/R_v + q_s} \frac{\partial q_s}{\partial T} \right) - \frac{g}{1 + q_t} \frac{\partial q_t}{\partial z}, \quad (1)$$

where g is gravitational acceleration, T is temperature, R_d and R_v are the gas constants of dry air and water vapor, respectively, q_s is the saturation mixing ratio, q_t is the total condensate mixing ratio, and Γ_m is the moist-adiabatic lapse rate:

$$\Gamma_m = g(1 + q_t) \left(\frac{1 + L_v q_s / R_d T}{c_{pm} + L_v \partial q_s / \partial T} \right), \quad (2)$$

where L_v is the latent heat of vaporization and c_{pm} is the specific heat of moist air at constant pressure. In the tropopause layer, q_s , $\partial q_s / \partial T$, and $\partial q_t / \partial z$ approach zero. In this limiting case, Eq. 1 reduces to:

$$N^2 = \frac{g}{\theta_v} \frac{\partial \theta_v}{\partial z}, \quad (3)$$

where θ_v is the virtual potential temperature. To compute N^2 , CM1 uses Eq. 1 in saturated environments and Eq. 3 in sub-saturated environments, but for simplicity only Eq. 3 will be used for the budget computations herein¹.

Taking the time derivative of Eq. 3 yields the static stability tendency:

$$\frac{\partial N^2}{\partial t} = \frac{g}{\theta} \frac{\partial}{\partial z} \frac{\partial \theta}{\partial t} - \frac{g}{\theta^2} \frac{\partial \theta}{\partial z} \frac{\partial \theta}{\partial t}, \quad (4)$$

¹The validity of this approximation will be substantiated later in this section.

71 where the potential temperature tendency, $\partial\theta/\partial z$, can be written:

$$\frac{\partial\theta}{\partial t} = HADV + VADV + HTURB + VTURB + MP + RAD + DISS \quad (5)$$

72 Each term on the right-hand side of Eq. 5 represents a potential temperature budget variable,
 73 each of which is output directly by the model every minute. HADV and VADV are the radial and
 74 vertical advective tendencies, HTURB and VTURB are the radial and vertical tendencies from
 75 the turbulence parameterization, MP is the tendency from the microphysics scheme, RAD is the
 76 tendency from the radiation scheme, and DISS is the tendency due to turbulent dissipation. This
 77 equation neglects Rayleigh damping, since this term is zero everywhere below 25 km, and the
 78 analysis domain does not extend to that level. Each term in Eq. 5 is substituted for $\partial\theta/\partial t$ in Eq.
 79 4, yielding the contribution of each budget term to the static stability tendency. These terms are
 80 summed, yielding an instantaneous "budget change" in N^2 every minute. The budget changes are
 81 then averaged over 24-hour periods and compared to the total model change in N^2 over that same
 82 time period using a residual, i.e.:

$$\Delta N_{budget}^2 = \sum_{t=t_0}^{t_0+\delta t} \frac{\partial N^2}{\partial t} |_{t, NEEDBAROVERSUMMATION} \quad (6)$$

$$\Delta N_{model}^2 = N_{t_0+\delta t}^2 - N_{t_0}^2, \quad (7)$$

$$Residual = \Delta N_{model}^2 - \Delta N_{budget}^2 \quad (8)$$

85 where t_0 is an initial time and δt is 24 hours. In Eq. 6, Eq. 1 in saturated environments and Eq. 3
 86 in sub-saturated environments; t_0 is an initial time and δt is 24 hours.

87 Eqs. 6-8 are plotted for four consecutive 24-hour periods in Fig. 1. For this and all subsequent
 88 radial-vertical cross sections, a 1-2-1 smoother is applied once in the radial direction to eliminate
 89 $2\Delta r$ noise that appears in some of the raw model output and calculated fields. The left column of
 90 Fig. 1 depicts the model changes (Eq. 7), the center column depicts the budget changes (Eq. 6),

91 and the right column depicts the residuals (Eq. 8). In every 24-hour period, the budget changes
92 are nearly identical to the model changes, which is reflected in the near-zero residuals in the
93 right column. This indicates that the budget accurately represents the model variability, which
94 implies that the neglect of moisture in the budget computation introduces negligible error within
95 the analysis domain².

96 In the tropopause layer, some of the budget terms are small enough to be ignored. To determine
97 which of the budget terms are most important, a time series of the contribution of each of the
98 budget terms in Eq. 5 to the tropopause-layer static stability tendency is plotted in Fig. 4. For this
99 figure, each of the budget terms is computed using the method described in Section 3, except with
100 1-hour averaging intervals instead of 24-hour intervals. The absolute values of these tendencies
101 are then averaged over the radius-height domain depicted in Fig. 1 and plotted as a time series³.
102 Advection (Fig. 4, red line) plays an important role in the mean tropopause-layer static stability
103 tendency at all times, and vertical turbulence (Fig. 4, blue line) and radiation (Fig. 4, dark green
104 line) both become important after 48 hours. Although the contribution from horizontal turbulence
105 (Fig. 4, purple line) becomes more important after 72 hours, it is confined to a very small region
106 immediately surrounding the eyewall tangential velocity maximum (not shown), and is negligible
107 throughout the rest of the tropopause layer. The remaining two processes - microphysics and
108 dissipative heating (Fig. 4, orange and light green lines, respectively) - lie atop one another near
109 zero. These time series indicate that, at all times, three budget terms dominate the tropopause-layer
110 static stability tendency: advection, vertical turbulence, and radiation. Variations in the magnitude

²This is not the case in the lower- and mid-troposphere, where the residual actually exceeds the budget variability in many places, likely due to the neglect of moisture; thus we limit this analysis to the upper troposphere and lower stratosphere.

³It will be seen in subsequent figures that each of the terms contributes both positively and negatively to the N^2 tendency within the analysis domain. Thus, taking an average over the domain tends to wash out the positive and negative contributions. To circumvent this problem, the absolute value of each of the terms is averaged, yielding a time series of the mean magnitude of each budget term.

111 and spatial structure of these terms drive the static stability changes depicted in Fig. 1; subsequent
112 sections will focus on these variations and what causes them.

113 **4. Results**

114 Don't forget to mention 1-2-1 smoother.

115 *a. Static stability evolution*

116 The average N^2 over the first day of the simulation (Fig. 3a) indicates the presence of a static
117 stability maximum about 400 m above the cold-point tropopause. This lower-stratospheric stable
118 layer had begun to erode during the initial spin-up period, with the maximum destabilization
119 occurring at the innermost radii. This decrease in static stability continued into the second day
120 of the simulation (Fig. 3b) as the storm intensified to hurricane strength (Fig. 2). Destabilization
121 was particularly pronounced over the developing eye, where the time-mean cold-point tropopause
122 height increased by up to 400 m compared to the previous day. Over the developing eyewall
123 and outer rainband regions, meanwhile, the tropopause height remained nearly constant. During
124 the third day of the simulation (Fig. 3c), static stability over the eye continued to decrease, and
125 the cold-point tropopause height rose to 18.3 km at the storm center. The tropopause sloped
126 sharply downward over the innermost radii, reaching the 16.4-km level near the 50-km radius. This
127 local minimum in tropopause height corresponded to the eyewall region, where upper-tropospheric
128 static stability increased during this time period. Outside of the eyewall region, static stability
129 began to increase in the layer immediately overlying the cold-point tropopause. This stable layer
130 sloped upward with radius, which corresponded to an upward-sloping tropopause radially outside
131 of the eyewall region. Over the next 24 hours (Fig. 3d), as the storm's maximum 10-m wind
132 speed leveled off near 80 m s^{-1} (Fig. 2), the upper-tropospheric static stability within the eyewall

133 region continued to strengthen, as did the static stability just above the cold-point tropopause
134 radially outside of the eyewall. As the stable layer strengthened, its altitude rose slightly, which
135 corresponded to a slight increase in tropopause height outside of the eyewall during this period.
136 Within the upper troposphere radially outside of the eyewall, meanwhile, static stability decreased
137 such that it was nearly neutral in a thin layer between the 120- and 150-km radii. The eye region
138 likewise continued to destabilize, and the cold-point tropopause height increased to a level above
139 18.5 km. This static stability evolution closely follows that observed in Hurricane Patricia (2015;
140 Duran and Molinari 2018).

141 *b. Static stability budget analysis*

142 *(i) 0-24 hours* The first 24 hours of the simulation was characterized by a weakening of the
143 lower-stratospheric static stability maximum above 17 km (Fig. ??a, purple shading) and an in-
144 crease in static stability below (green shading). Although these tendencies extended out to the
145 200-km radius, they were particularly pronounced at innermost radii. A comparison of the contri-
146 butions of advection (Fig. ??b), vertical turbulence (Fig. ??c), and radiation (Fig. ??d) reveals that
147 advection is primarily responsible for the change in static stability during this period. ...Explain
148 this in the context of radial and vertical velocities...

149 *(ii) 24-48 hours* During the second day of the simulation, the lower-stratospheric stable layer
150 continued to weaken (Fig. 6a). This weakening trend in the 16.75-17.75-km layer extended from
151 the 50 km radius outward to past 200 km, and was primarily driven by advection (Fig. 6b). Below
152 this layer, static stability began to increase slightly. This stabilization had contributions from both
153 vertical turbulence (Fig. 6c) and radiation (Fig. 6d) in the 16-16.5-km layer. ...Explain this in
154 context of mean vertical mixing coefficient and mean radiative heating tendency... Meanwhile,

155 radially inward of 60 km, static stability below 17.5 km continued to weaken, primarily due to
156 advective processes.

157 *(iii) 48-72 hours* The third day of the simulation marked a dramatic change in the structure of the
158 tropopause-layer static stability tendencies. During this time, static stability increased markedly
159 in an upward-sloping region within the 30-60-km radial band (Fig. 7a), and also increased within
160 the 16.75-17.5-km layer out to at least the 200-km radius. As this layer stabilized, the layer
161 immediately below it destabilized in a broad region extending from 60-200 km. Examination
162 of the contribution from total advection (Fig. 7b) reveals that advection no longer dominates the
163 static stability tendencies. Instead, a combination of vertical turbulence (Fig. 7c) and radiation
164 (Fig. 7d) overcomes the destabilizing influence of advection to create the layer of increasing static
165 stability. Meanwhile, the destabilizing influence of vertical turbulence in a broad region below
166 17 km combines with a small region of destabilization due to radiation in the 50-120-km radial
167 band combine to destabilize the layer below 16.5 km in the 50-200-km radial band. Comparing
168 the sum of advection and vertical turbulence (Fig. 7e) to the sum of advection, vertical turbulence,
169 and radiation (Fig. 7f) reveals that radiation plays a fundamental role in the re-strengthening of the
170 lower-stratospheric stable layer during this time.

171 *(iv) 72-96 hours*

172 **5. Discussion**

173 Dunion et al. speculate that the diurna pulse only occurs in mature storms. Maybe the develop-
174 ment of the near-tropopause stable layer could partially explain the reason for this.

175 *Acknowledgments.* We are indebted to Dr. George Bryan for his continued development and
176 support of Cloud Model 1. We also thank Drs. Jeffrey Kepert, Robert Fovell, and Erika Navarro
177 for fruitful conversations related to this work. ADD GRANT NUMBER

178 **References**

179 Bell, M. M., and Coauthors, 2016: Office of Naval Research Tropical Cyclone Intensity (TCI)
180 2015 NASA WB-57 High Density Dropsonde Sounding System (HDSS) data, version 1.0. doi:
181 10.5065/D6KW5D8M.

182 Bryan, G. H., 2012: Effects of surface exchange coefficients and turbulence length scales on the
183 intensity and structure of numerically simulated hurricanes. *Mon. Wea. Rev.*, **140**, 1125–1143.

184 Bryan, G. H., and R. Rotunno, 2009: The maximum intensity of tropical cyclones in axisymmetric
185 numerical model simulations. *Mon. Wea. Rev.*, **137**, 1770–1789.

186 Doyle, J. D., and Coauthors, 2017: A view of tropical cyclones from above: The Tropical Cyclone
187 Intensity (TCI) Experiment. *Bull. Amer. Meteor. Soc.*, **98**, 2113–2134.

188 Dunion, J. P., C. D. Thorncroft, and C. S. Velden, 2014: The tropical cyclone diurnal cycle of
189 mature hurricanes. *Mon. Wea. Rev.*, **142**, 3900–3919.

190 Duran, P., and J. Molinari, 2018: Dramatic inner-core tropopause variability during the rapid
191 intensification of Hurricane Patricia (2015). *Mon. Wea. Rev.*, **XXX**, XXX–XXX.

192 Iacono, M. J., J. S. Delamere, E. J. Mlawer, M. W. Shephard, S. A. Clough, and W. D. Collins,
193 2008: Radiative forcing by long-lived greenhouse gases: Calculations with the AER radiative
194 transfer models. *J. Geophys. Res.*, **113** (D13103).

195 Kimberlain, T. B., E. S. Blake, and J. P. Cangialosi, 2016: Tropical cyclone report: Hurricane
 196 Patricia. National Hurricane Center. [Available online at www.nhc.noaa.gov].
 197 Markowski, P. M., and G. H. Bryan, 2016: LES of laminar flow in the PBL: A potential problem
 198 for convective storm simulations. *Mon. Wea. Rev.*, **144**, 1841–1850.
 199 Rogers, R. F., S. Aberson, M. M. Bell, D. J. Cecil, J. D. Doyle, J. Morgerman, L. K. Shay, and
 200 C. Velden, 2017: Re-writing the tropical record books: The extraordinary intensification of
 201 Hurricane Patricia (2015). *Bull. Amer. Meteor. Soc.*, **98**, 2091–2112.
 202 Rotunno, R., and K. A. Emanuel, 1987: An air-sea interaction theory for tropical cyclones. Part II:
 203 Evolutionary study using a nonhydrostatic axisymmetric numerical model. *J. Atmos. Sci.*, **44**,
 204 542–561.
 205 Thompson, G., R. M. Rasmussen, and K. Manning, 2004: Explicit forecasts of winter precipitation
 206 using an improved bulk microphysics scheme. Part I: Description and sensitivity analysis. *Mon.*
 207 *Wea. Rev.*, **132**, 519–542.

LIST OF FIGURES

209	Fig. 1.	Left panels: Twenty-four-hour changes in squared Brunt-Väisälä frequency ($N^2 \cdot 10^{-4} \text{ s}^{-2}$) over (a) 0-24 hours, (b) 24-48 hours, (c) 48-72 hours, (d) 72-96 hours. Middle Panels: The N^2 change over the same time periods computed using Eq. ?? Right Panels: The budget residual over the same time periods, computed by subtracting the budget change (middle column) from the model change (left column).	14
210			
211			
212			
213			
214	Fig. 2.	The maximum 10-m wind speed (top panel; m s^{-2}) and minimum sea-level pressure (bottom panel; hPa) in the simulated storm (blue lines) and from Hurricane Patricia's best track (red stars).	15
215			
216			
217	Fig. 3.	Twenty-four-hour averages of squared Brunt-Väisälä frequency (10^{-4} s^{-2}) over the first four days of the simulation. Orange lines represent the cold-point tropopause computed from the mean temperature field over the same time periods.	16
218			
219			
220	Fig. 4.	Time series of the contribution of each of the budget terms to the time tendency of the squared Brunt-Väisälä frequency (N^2 ; 10^{-4} s^{-2}). For each budget term, the absolute value of the N^2 tendency is averaged both temporally over 1-hour periods (using output every minute), and spatially within the radius-height domain depicted in Fig. ??	17
221			
222			
223			
224	Fig. 5.	(a) Total change in N^2 over the 0-24-hour period ($10^{-4} \text{ s}^{-2} (24 \text{ hr})^{-1}$) and the contributions to that change from (b) the sum of horizontal and vertical advection, (c) vertical turbulence, and (d) the sum of longwave and shortwave radiation.	18
225			
226			
227	Fig. 6.	As in Fig. 5, but for the 24-48-hour period.	19
228			
229	Fig. 7.	(a) Total change in N^2 over the 48-72-hour period ($10^{-4} \text{ s}^{-2} (24 \text{ hr})^{-1}$) and the contributions to that change from (b) the sum of horizontal and vertical advection, (c) vertical turbulence, (d) the sum of longwave and shortwave radiation, (e) the sum of horizontal advection, vertical advection, and vertical turbulence, and (f) the sum of horizontal advection, vertical advection, vertical turbulence, and longwave and shortwave radiation.	20
230			
231			
232			
233	Fig. 8.	As in Fig. 7, but for the 72-96-hour period.	21
234			
235	Fig. 9.	Radial velocity (m s^{-1} ; filled contours), potential temperature (K; thick black contours), and cold point tropopause height (orange line) averaged over (a) 0-24 hours, (b) 24-48 hours, (c) 48-72 hours, and (d) 72-96 hours.	22
236			
237	Fig. 10.	Vertical velocity (cm s^{-1} ; filled contours), potential temperature (K; thick black contours), and cold point tropopause height (orange line) averaged over (a) 0-24 hours, (b) 24-48 hours, (c) 48-72 hours, and (d) 72-96 hours.	23
238			
239			
240	Fig. 11.	Total condensate mixing ratio (g kg^{-1}) and cold point tropopause height (orange line) averaged over (a) 0-24 hours, (b) 24-48 hours, (c) 48-72 hours, and (d) 72-96 hours.	24
241			

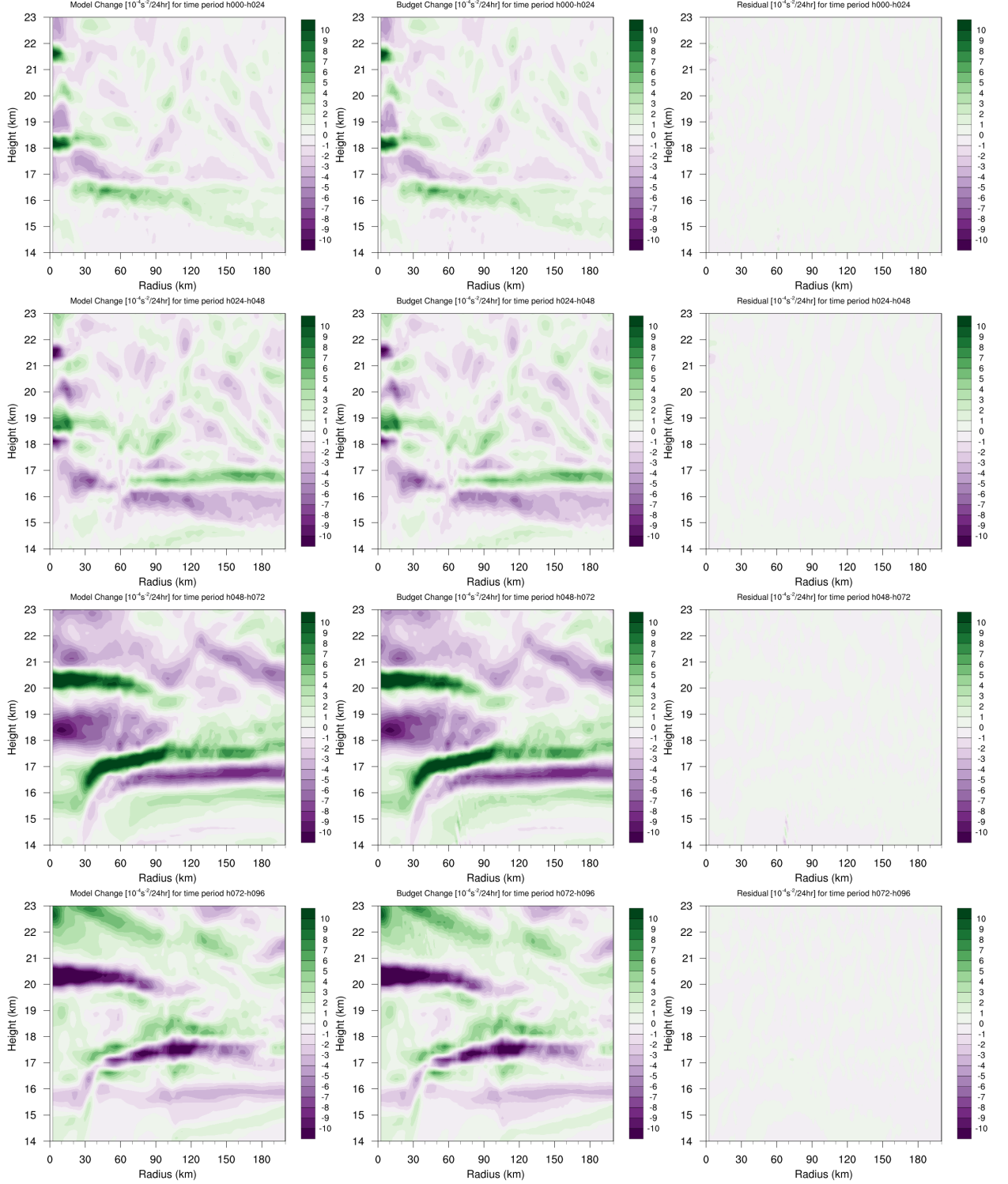


FIG. 1. Left panels: Twenty-four-hour changes in squared Brunt-Väisälä frequency ($N^2 \text{ } 10^{-4} \text{ s}^{-2}$) over (a) 0-24 hours, (b) 24-48 hours, (c) 48-72 hours, (d) 72-96 hours. Middle Panels: The N^2 change over the same time periods computed using Eq. ?? Right Panels: The budget residual over the same time periods, computed by subtracting the budget change (middle column) from the model change (left column).

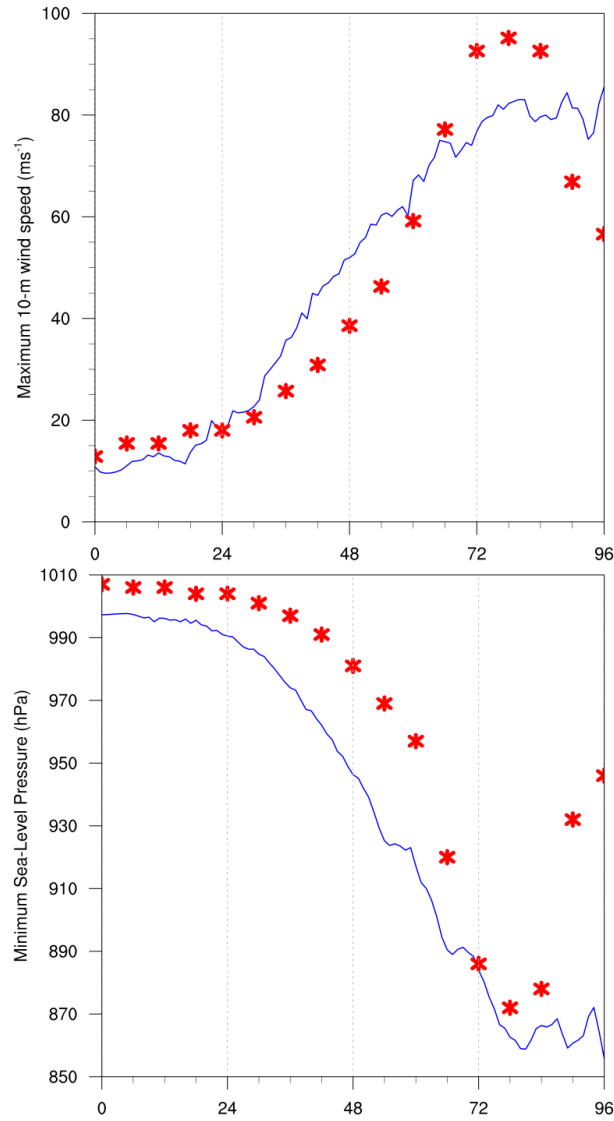


FIG. 2. The maximum 10-m wind speed (top panel; m s^{-2}) and minimum sea-level pressure (bottom panel; hPa) in the simulated storm (blue lines) and from Hurricane Patricia's best track (red stars).

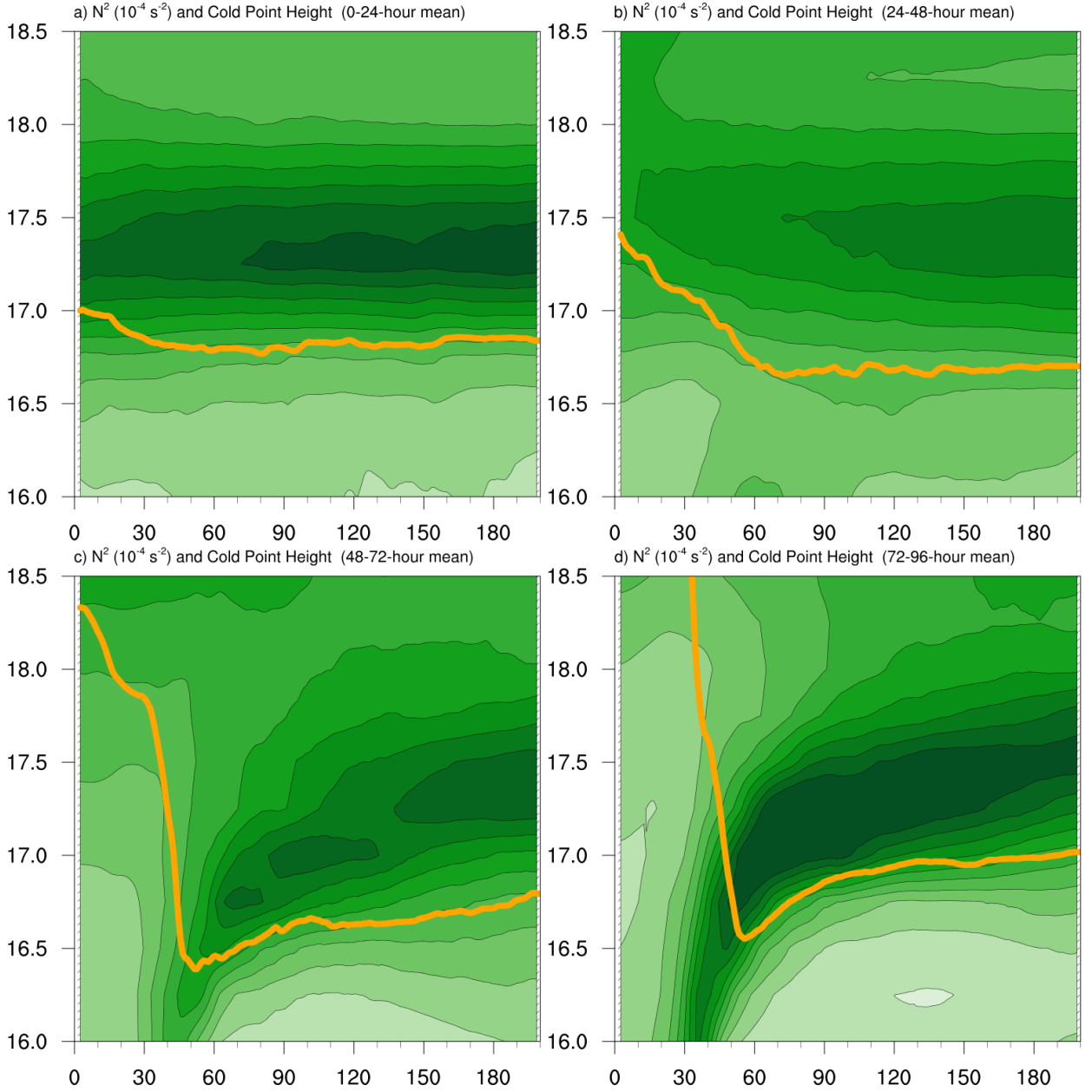


FIG. 3. Twenty-four-hour averages of squared Brunt-Väisälä frequency (10^{-4} s^{-2}) over the first four days of the simulation. Orange lines represent the cold-point tropopause computed from the mean temperature field over the same time periods.



figures/fig04_AVG_budterms.png

251 FIG. 4. Time series of the contribution of each of the budget terms to the time tendency of the squared
252 Brunt-Väisälä frequency (N^2 ; 10^{-4} s^{-2}). For each budget term, the absolute value of the N^2 tendency is averaged
253 both temporally over 1-hour periods (using output every minute), and spatially within the radius-height domain
254 depicted in Fig. ??.

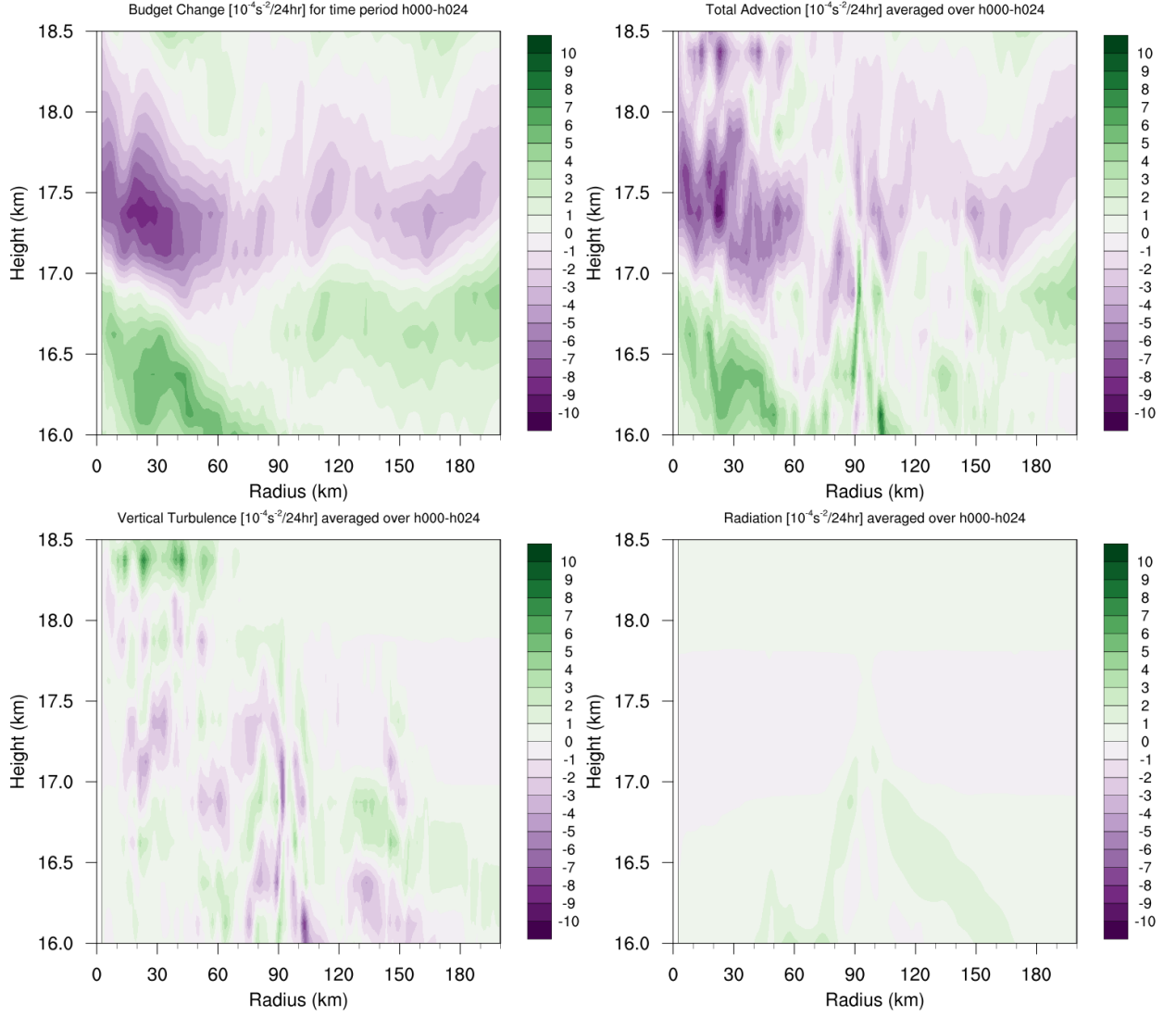


FIG. 5. (a) Total change in N^2 over the 0-24-hour period ($10^{-4} \text{ s}^{-2} (24 \text{ hr})^{-1}$) and the contributions to that change from (b) the sum of horizontal and vertical advection, (c) vertical turbulence, and (d) the sum of longwave and shortwave radiation.

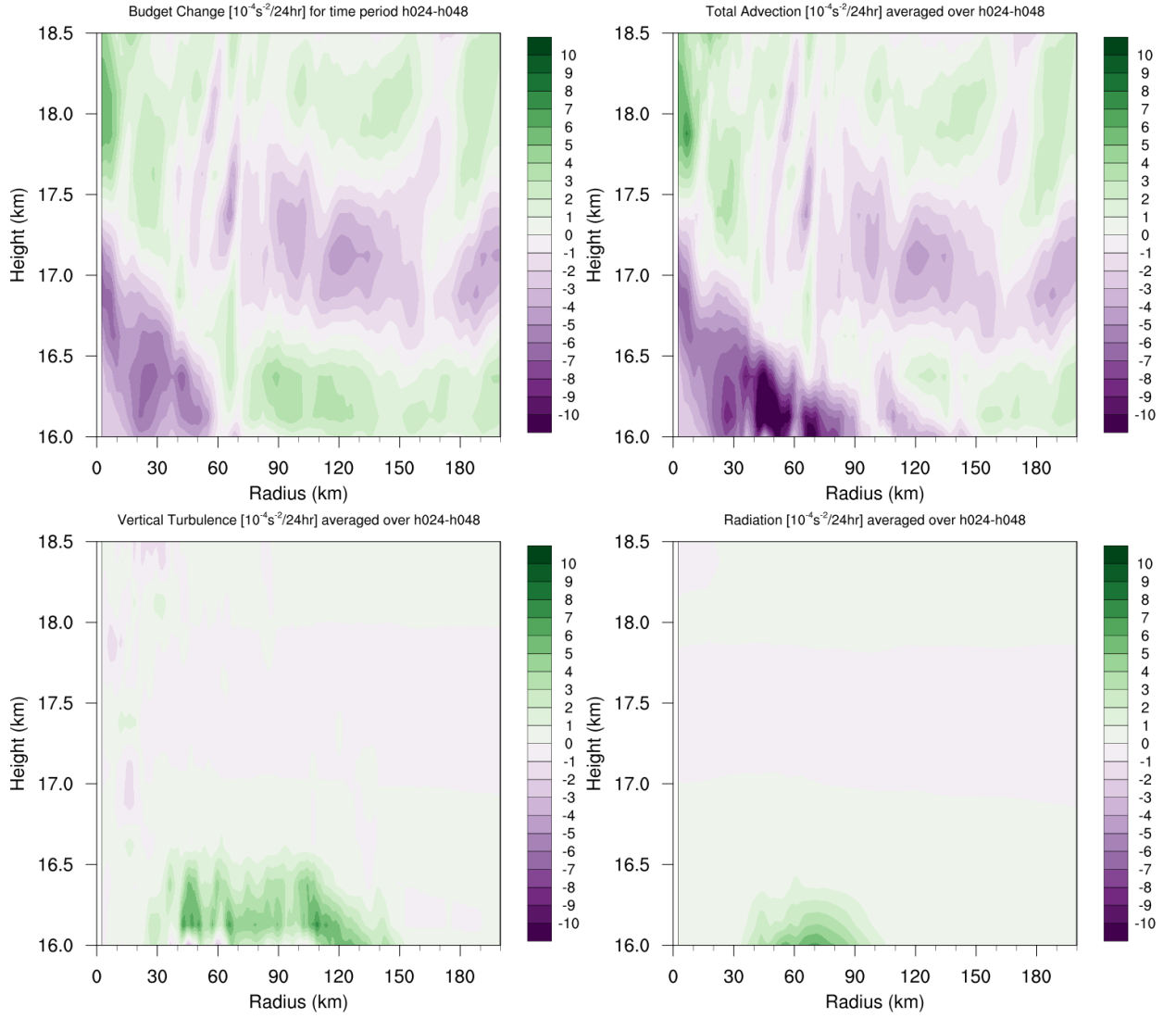



FIG. 6. As in Fig. 5, but for the 24-48-hour period.



figures/fig07_h048-h072-budgetterms.png

258 FIG. 7. (a) Total change in N^2 over the 48-72-hour period (10^{-4} s^{-2} (24 hr^{-1})) and the contributions to that
259 change from (b) the sum of horizontal and vertical advection, (c) vertical turbulence, (d) the sum of longwave
260 and shortwave radiation, (e) the sum of horizontal advection, vertical advection, and vertical turbulence, and (f)
261 the sum of horizontal advection, vertical advection, vertical turbulence, and longwave and shortwave radiation.

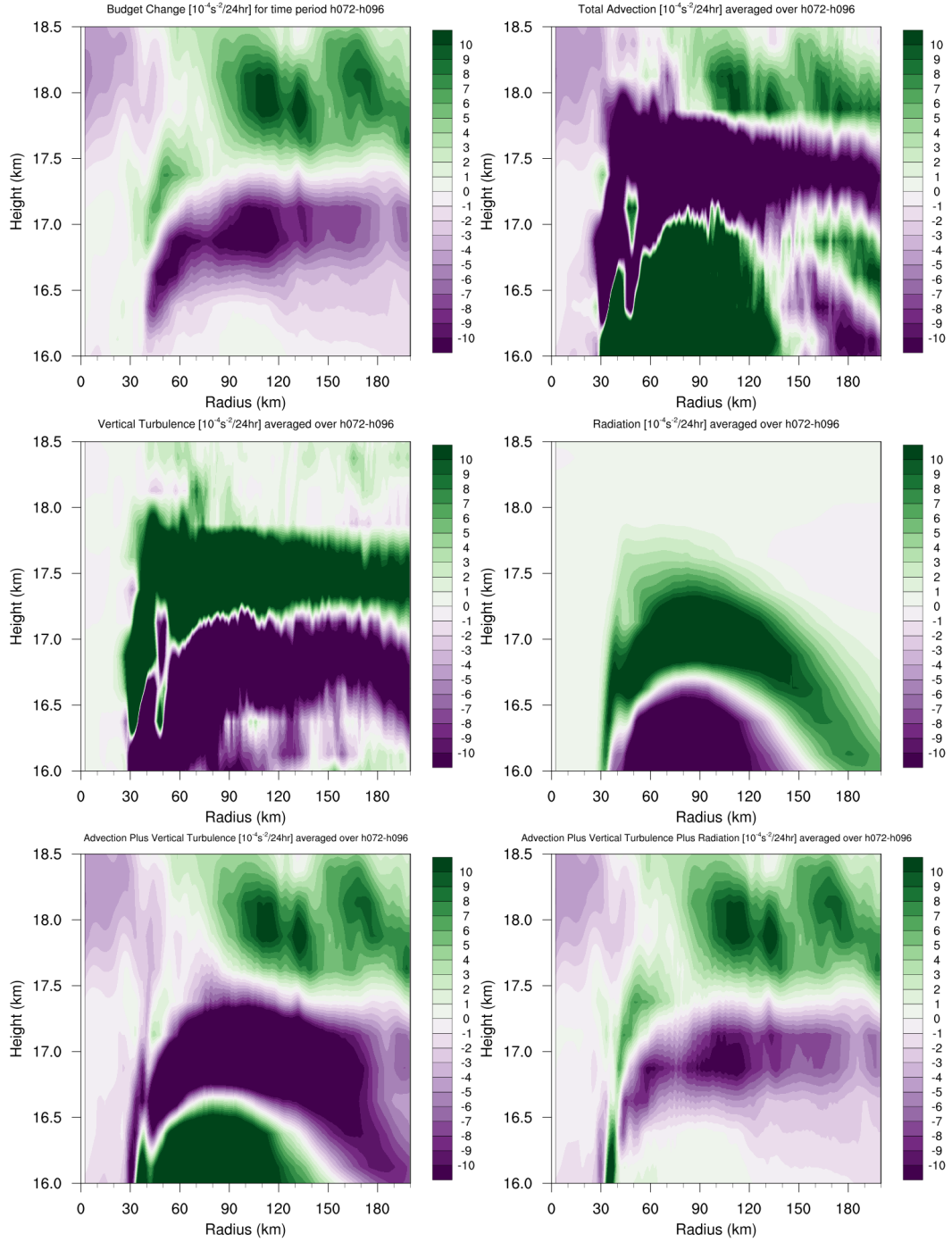


FIG. 8. As in Fig. 7, but for the 72-96-hour period.

figures/fig09_u.png

262 FIG. 9. Radial velocity (m s^{-1} ; filled contours), potential temperature (K; thick black contours), and cold point
263 tropopause height (orange line) averaged over (a) 0-24 hours, (b) 24-48 hours, (c) 48-72 hours, and (d) 72-96
264 hours.

figures/fig10_w.png

265 FIG. 10. Vertical velocity (cm s^{-1} ; filled contours), potential temperature (K; thick black contours), and cold
266 point tropopause height (orange line) averaged over (a) 0-24 hours, (b) 24-48 hours, (c) 48-72 hours, and (d)
267 72-96 hours.

figures/fig11_qtot.png

268 FIG. 11. Total condensate mixing ratio (g kg^{-1}) and cold point tropopause height (orange line) averaged over
269 (a) 0-24 hours, (b) 24-48 hours, (c) 48-72 hours, and (d) 72-96 hours.